

---

# Investigation of the characteristics of low-level jets over North America in a convection-permitting WRF simulation

Xiao Ma<sup>1,2</sup>, Yanping Li<sup>1,2</sup>, Zhenhua Li<sup>1</sup>, Fei Huo<sup>1</sup>

<sup>1</sup>Global Institute for Water Security, University of Saskatchewan, 11 Innovation Blvd, Saskatoon, SK, S7N 3H5, Canada

<sup>2</sup>School of Environment and Sustainability, University of Saskatchewan, 117 Science Place, Saskatoon, SK, S7N 5C8, Canada

*Correspondence to:* Yanping Li (yanping.li@usask.ca)

**Abstract.** In this study, we utilized a high-resolution (4 km) convection-permitting Weather Research Forecasting (WRF) simulation spanning a 13-year period (2000-2013) to investigate the climatological features of Low-level Jets (LLJs) over North America. The 4-km simulation enabled us to represent the effects of orography and the underlying surface on the boundary layer winds better. Focusing on the continental US and the adjacent border regions of Canada and Mexico, this study not only identified several well-known large-scale LLJs such as the southerly Great Plains LLJ and the summer northerly California coastal LLJ, but also the winter Quebec northerly LLJ which gets less focus before. All these LLJs reach the strongest in the night time in the diurnal cycle. Thus, the different thermal and dynamic mechanisms forming these three significant LLJs are investigated in this paper: Inertial oscillation theory dominates in Great Plain LLJ, California coastal LLJ is formed by the baroclinic theory, whereas the Quebec LLJ is associated with both theories. Moreover, the high-resolution simulation revealed climatic characteristics of weaker and smaller-scale LLJs or low-level wind maxima in regions with complex terrains, such as the northerly LLJs in the foothill regions of the Rocky Mountains and the Appalachian during the winter. This study provides valuable insights into the climatological features of LLJs in North America and the high-resolution simulation offers a more detailed understanding of LLJ behavior near complex terrains and other smaller-scale features.

---

## 25 1. Introduction

26 A low-level jet (LLJ) is described as the fast-moving air ribbon located in the lower atmosphere most of the time  
27 (Bonner, 1968; Rife et al., 2010). Many of the world's LLJs have been studied, such as the Great Plains LLJ over the  
28 central US (Bonner, 1968; Zhong et al., 1996), the Somali LLJ over eastern Africa (Munday et al., 2021), and the  
29 South American LLJ over the east Andes Mountains (Montini et al., 2019). Other studies extend beyond in-land LLJs  
30 to encompass offshore coastal LLJs such as the California LLJs (Parish, 2000) and North African Coastal LLJ (Soares  
31 et al., 2018). A kind of mesoscale weather system, an LLJ has a relatively small vertical range of usually only a few  
32 hundred meters, but its width can reach several hundred kilometers. LLJs are closely related to precipitation and even  
33 extreme events, and they can transfer abundant water vapor to the downwind regions, providing favorable dynamic  
34 conditions for rainfall (Walters and Winkler, 2001; Hodges and Pu, 2019). Meanwhile, researchers have long been  
35 interested in investigating their features, because LLJs also affect various processes such as wind power development,  
36 air pollution transportation, and urban heat islands: the wind turbines would be influenced by positive wind shear and  
37 downward entrainment from the LLJs above them, assisting in extracting energy from the strong wind belt inside LLJs  
38 (Gadde and Stevens 2021; Ma et al., 2022). LLJ-related horizontal transportation is beneficial to pollutant removal  
39 (Sullivan et al. 2017). The LLJs can enhance the turbulent mixing in the boundary layer thereby decreasing the  
40 atmospheric stability, helping pollution diffusion, and weakening urban heat island intensity (Hu et al., 2013).

41 Since the mid-20th century, scientists have used regular rawinsonde observations to investigate the characteristics of  
42 LLJs. Applying rawinsondes to investigate the Great Plains LLJ in the central US, Bonner (1968), Mitchell et al.  
43 (1995), and Walters et al. (2008) studied its distribution, seasonal activity, horizontal and vertical structure, and diurnal  
44 features and established the climatology of the Great Plains LLJ during warm seasons. As well as rawinsondes, radar  
45 systems and wind profilers are useful tools for characterizing LLJs. Frisch et al. (1992) observed a typical LLJ process  
46 using Doppler weather radar in North Dakota and identified that the friction on the surface of the boundary layer is  
47 important in the early stages of LLJ development. Using long-term wind profiler measurement, Miao et al. (2018)  
48 interpreted the climatology of LLJs in Beijing and Guangzhou, concluding that the frequency values of LLJs in these  
49 two cities are 13.0% and 4.9%, respectively. Moreover, Smith et al. (2019) used the Plains Elevated Convection at  
50 Night (PECAN) observations to conduct high-quality measurements of nocturnal LLJs with wide spatial and temporal  
51 resolutions. They found that sudden changes in LLJ structure typically result from the spatial evolution of the LLJ.

---

52 However, there are some disadvantages of observational research that should be noted. First, regular rawinsonde data  
53 only contain measurements at two daily time points (00 UTC and 12 UTC), which cannot fully capture LLJs' diurnal  
54 variations. The time density of observations is therefore coarse, and coastal areas lack regular high-density  
55 measurements, making the study of coastal LLJs challenging (Mitchell et al., 1995). Second, heterogeneities in the  
56 rawinsonde records, such as variations in station locations, radiosonde types, and archiving procedures, may also  
57 complicate the use of these observations in climate research. Third, rawinsonde measurements taken at a single point  
58 are not able to capture horizontal shear and environmental conditions (Chen et al., 2005). Although observation  
59 platforms such as radar, PECAN, or lidar which investigate the atmosphere as low as 300 m, can compensate to some  
60 extent for this lack of observational data. as well as lidar that investigates the atmosphere as low as 300 m, these  
61 approaches are still limited by the spatial coverage of their measurement platforms (Smith et al., 2019).

62 Because of these problems with observational methods, researchers have chosen reanalysis datasets as an alternative  
63 for investigating LLJs. Reanalysis data have relatively better spatial and temporal coverage than rawinsonde  
64 measurements, incorporate observations into the preliminary model simulations, provide more comprehensive  
65 variables through assimilation, and contain broader domains. Rife et al. (2010) highlighted the global distribution of  
66 identified nocturnal LLJs using reanalysis data with a horizontal grid spacing of 40 km, and even successfully  
67 extracted some previously unknown jets, like Tarim nocturnal LLJ in northwest China, Ethiopia nocturnal LLJ, and  
68 Namibia–Angola nocturnal LLJ. Doubler et al. (2015) applied the North American Regional Reanalysis (NARR)  
69 dataset (~32 km) to generate long-term LLJ climatology in North America. Consistent with previous records,  
70 Doubler's results supplemented the description of some smaller-scale LLJs. Similarly, Montini et al. (2019) compared  
71 and validated the performance of five different reanalysis datasets in identifying LLJs. Their results showed the 38-  
72 year climatology of South American LLJs with ERA-Interim data (~79 km).

73 Scientists have also conducted studies based on numerical simulations, which can more accurately represent LLJs than  
74 reanalysis data sets, especially in the vertical direction, thereby yielding new insights into LLJs' features. Tang et al.  
75 (2017) used an ensemble of dynamically downscaling regional climate simulations to generate the climatology of  
76 Great Plains LLJ and predicted that the LLJ will occur more frequently during the nighttime in spring and summer in  
77 mid-21st century. Jiménez-Sánchez et al. (2019) conducted a simulation for LLJs over the Orinoco River Basin by  
78 dynamic downscaling of the Weather Research and Forecasting model (WRF). The simulation represented the jet

---

79 streaks better than previous studies within a broader region of wind enhancement and illustrated more detailed diurnal  
80 evolution. Nevertheless, most general numerical simulations still represent the convective processes by the  
81 parameterization scheme, which generates uncertainty in the results. These issues can be addressed by using  
82 convection-permitting models with grid spacing under 5 km that adequately simulate the convections and other small-  
83 scale processes (Liu et al., 2017, Li et al., 2019, Kurkute et al., 2020). Convection-permitting modeling describes the  
84 underlying surface more accurately than coarse-resolution simulations and reanalysis data and shows ability in  
85 investigations of LLJs near complex mountain areas. Du and Chen (2019) analyzed the LLJs over southern China by  
86 using 4-km WRF model and revealed a solid relationship between the mesoscale lifting of LLJs and the convection's  
87 initiation. They also highlighted the importance of coastal terrain. Overall, the finer-resolution tools tend to show more  
88 comprehensive and precise results, offering detailed and accurate references to LLJs.

89 The formation mechanisms of LLJs have been studied extensively by researchers. In explaining the diurnal cycle  
90 feature of the Great Plains LLJ, the inertial oscillation theory proposed by Blackadar (1957) and Stensrud (1996)  
91 suggests that the LLJ is related to the friction change in the boundary layer. During the night, the jet-core wind is  
92 enhanced after decoupling with near-surface friction. Holton (1967) and Parish (2000) developed the thermal wind  
93 adjustment theory, which suggests that the horizontal pressure gradient changes because the atmosphere over sloping  
94 terrain is warmer or because sea-land contrast influences the diurnal cycle of wind. Additionally, LLJs can also be  
95 formed due to synoptic system forcing, as proposed by Uccellini et al. (1987) and Saulo et al. (2007). However,  
96 convection-permitting models can help explain how LLJs form because they have precise descriptions of weather  
97 systems and underlying orography. Using 4-km simulations, Fu et al. (2018) and Zhang et al. (2019) analyzed the  
98 evolution of LLJs over mountainous areas in eastern and southwestern China, respectively. They concluded that  
99 inertial oscillation plays a prominent role in and is responsible for the local precipitation peak at a certain time. Besides,  
100 Shapiro et al. (2016) argued that the formation of some LLJs may not be impacted by a single factor and that a unified  
101 theory analysis is thus required. Thus, a dataset that offers more information must be very popular. All these studies  
102 have shown that convection-permitting models, with both finer coverage and resolutions, are a powerful tool for LLJ  
103 characteristics research.

104 In this study, we utilize the 4-km convection-permitting WRF simulation (Liu et al., 2017) to analyze the features of  
105 low-level jet systems across North America, improving the spatial and temporal resolutions. Section 2 introduces the

---

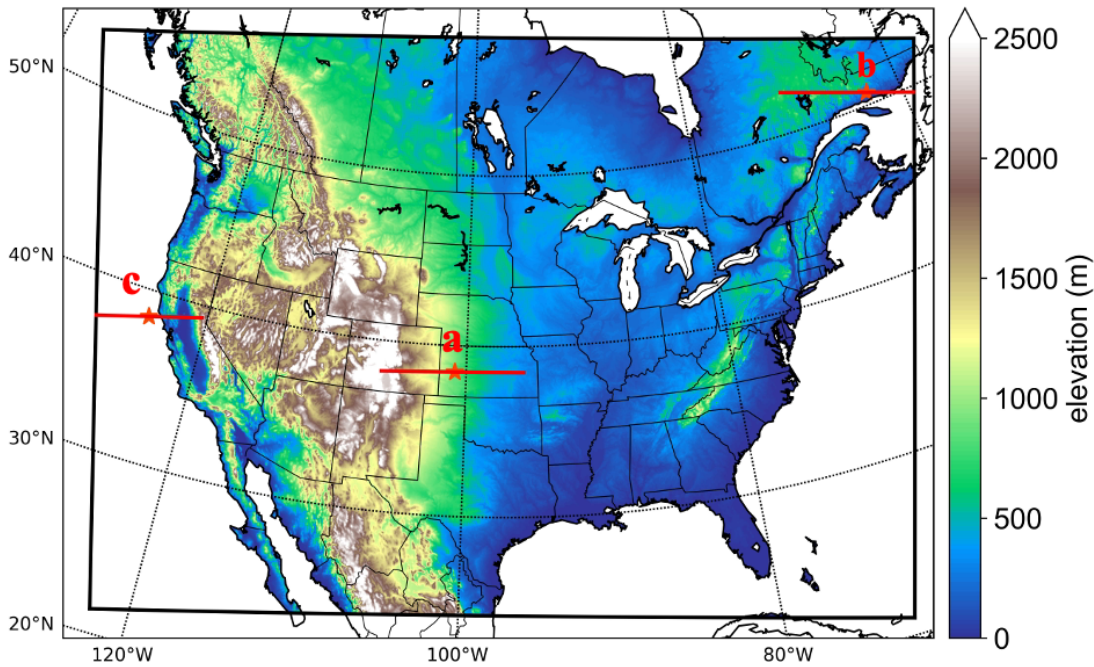
106 model configuration and the criteria for LLJ identification, Section 3 presents the characteristics of LLJ frequencies  
107 in North America, and Section 4 illustrates the analysis of the background and mechanisms in several LLJ cases.  
108 Finally, Section 5 provides the discussion and conclusion.

## 109 **2. Model configuration and methods**

### 110 **2.1 WRF setup**

111 This study utilized a convection-permitting Weather Research and Forecasting (WRF) dataset (Liu et al. 2017, Data  
112 available at: <https://rda.ucar.edu/datasets/ds612.0/>) with a horizontal resolution of 4 km over North America, without  
113 nesting. The domain covers the entire continental US, Southern Canada, and Northern Mexico, as illustrated in Figure  
114 1. The simulation provides three-dimensional data at a temporal resolution of 3 hours, resulting in 8-time steps per  
115 day. In the vertical direction, the data have 51 eta levels and can reach 50 hPa. It should be noted that there are five  
116 layers under 500-m height and nine layers under 1 km are outputted above ground level, which means the WRF has a  
117 better ability than other coarse modelling, to capture the LLJs occurring in the boundary layer. Considering the  
118 computational cost for high-resolution modelling, this simulation period spans from 1st October 2000 to 30th  
119 September 2013, and the six-hourly ERA-Interim reanalysis dataset of  $0.7^\circ$  resolution was used as input for the climate  
120 simulation, the vertical layer depth of the forcing ERA-Interim data under 5 km is about 0.3-1.4 km (Hoffmann &  
121 Spang, 2022). Even though the version is older, the ERA-Interim dataset still has been maturely applied in the climate  
122 modelling study and accumulating a wealth of related cases and experiences (Liu et al., 2017, Li et al., 2019). Besides,  
123 it is noted that 13 years is shorter than the normally defined climatology, but considering the computational cost of  
124 high-resolution simulation, it is still a balanced compromise. This shorter period length was also utilized to analyze  
125 the climate features of other weather events (Liu et al., 2017, Ma et al., 2022). The simulation did not apply any  
126 cumulus parameterization scheme due to the fine horizontal grid spacing, but other sub-grid scale processes were  
127 parameterized by various physical schemes: the rapid radiative transfer model (RRTMG) (Iacono et al., 2008) was  
128 used for simulating longwave and shortwave radiations, the Yonsei University (YSU) scheme was used for  
129 representing the planetary boundary layer (Hong et al., 2006), and the Noah-MP model was used for computing surface  
130 processes (Niu et al., 2011). In this study, the planetary boundary layer scheme is retained. Nonetheless, it should be

131 noted that this would introduce uncertainties to the simulation in the vertical direction, especially in regions with  
132 complex topography.



133  
134 **Figure 1. Study domain of this convection-permitting model. The colors represent the elevation. The red lines and stars**  
135 **show the positions of investigated cross-section and jets in Section 4.**

136  
137 **2.2 Methodology**

138 Using the threshold criteria proposed by Bonner (1968), this study identifies LLJs from the vertical wind profile of  
139 each grid point in the model output data. LLJs are present when the following conditions are met: (1) the height of the  
140 LLJ core maximum wind speed is below 3 km above the ground level (AGL); (2) the maximum wind speed is greater  
141 than or equal to 12 m s<sup>-1</sup>; (3) from the height of the wind maxima to the height of the next minimum value or 3-km  
142 height (whichever is lower), the velocity of winds drop by at least 6 m s<sup>-1</sup>; (4) the wind speed drops by at least 6 m s<sup>-1</sup>  
143 1 below the level of wind maxima. On the other hand, the investigation of LLJs is normally conducted with different  
144 jet-core wind directions. Pu and Cook (2010) studied the West African Westerly Jet, this zonal LLJ can help transport  
145 water vapor from the Atlantic to Africa, this LLJ is related to the westward extension of the continental thermal low  
146 pressure over Africa in summer. Thus, the LLJ research should refer to the local climatologic or geographic features.  
147 Considering the importance of the meridional LLJ for heat and water vapor transport over North America, as well as

---

148 the direction of the Rockies, this study addresses LLJ frequencies in different meridional directions. According to  
149 Walter et al. (2008) and Doubler et al. (2015), the criteria for identifying different meridional LLJs are as follows: for  
150 southerly LLJs (S-LLJs), the jet-core wind direction is between  $113^\circ$  and  $247^\circ$ ; for northerly LLJs (N-LLJs), the jet-  
151 core direction is between  $293^\circ$  and  $67^\circ$ . These criteria are also used in this study.

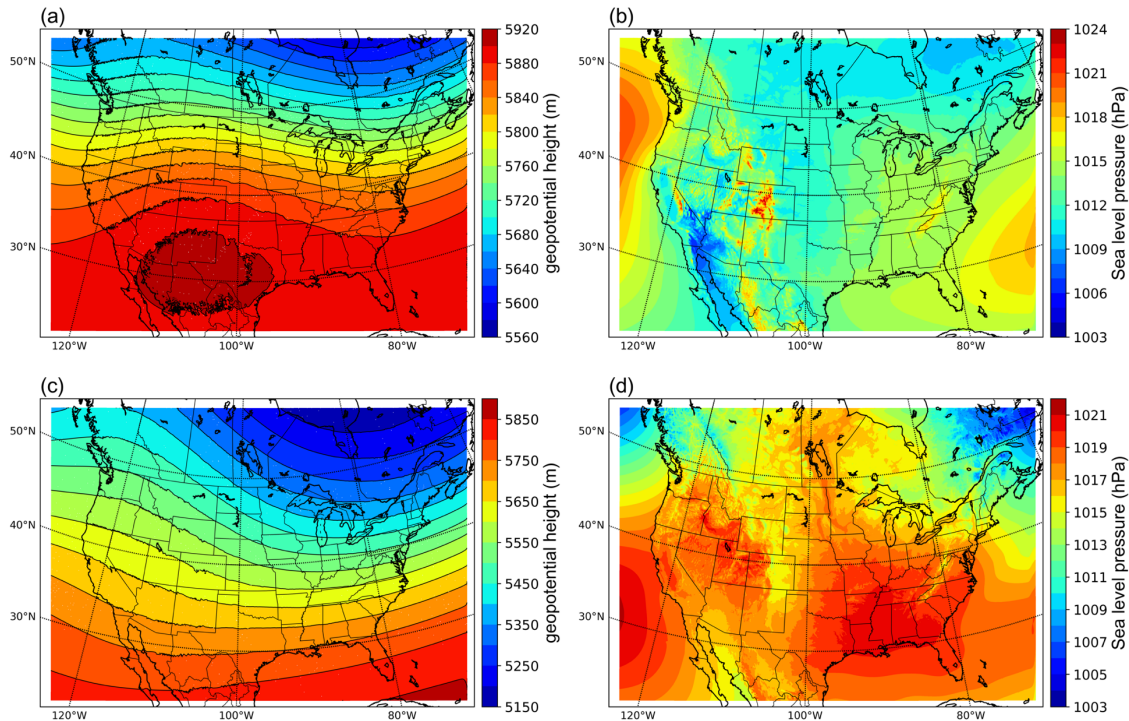
152 Based on the identification criteria above, we determined if the LLJ existed at each grid point and consequently  
153 counted the occurrences of S-LLJs and N-LLJs. We also calculated the frequencies of LLJs in different seasons or  
154 time steps. The frequency is defined as the percentage of the total number of occurrences for the selected accumulation  
155 period. We generated the frequency distribution maps for LLJs in North America, which are illustrated in Section 3.

### 156 **3. The patterns of North American LLJs**

#### 157 **3.1 Analysis of atmospheric circulation**

158 This study adopts model data to capture the climatological features of LLJs in North America. Considering the  
159 relationship between LLJs and synoptical systems, we evaluated the ability of the convection-permitting model to  
160 simulate the background atmospheric circulation. Figure 2 depicts the simulated multi-year analysis of geopotential  
161 heights at 500 hPa and sea-level pressure isobars for summer and winter. In summer, at a height of 500 hPa (Figure  
162 2a), In summer, the model depicts a trough in the east of the continental US, a ridge over the Rocky Mountains, and  
163 the upper-air subtropical anticyclone crossing the southern US. At sea level (Figure 2b), the model captures the Azores  
164 High-Pressure area in the Atlantic Ocean and the Hawaiian High-Pressure area in the Pacific.

165 In winter, the contours at the pressure value of 500 hPa (Figure 2c) show stronger fluctuating characteristics: the  
166 eastern trough and western ridge over the continent strengthen, and the polar vortex extends to the northern US, while  
167 most of North America is controlled by a cold high-pressure system. In addition, the subtropical anticyclone is too  
168 weak to be found within the study domain. On the other hand, most of North America is controlled by a cold high-  
169 pressure system at sea level (Figure 2d), and parts of the Icelandic Low and Aleutian Low appear on both east and  
170 west of Canada, even though their centers are not captured in the domain. To summarize, the convection-permitting  
171 model can simulate the features of semi-permanent centers of atmospheric circulations in North America, thus  
172 demonstrating its strength in identifying the LLJs in this area.



173  
 174 **Figure 2. Multi-year patterns of atmospheric circulations simulated by the convection-permitting model: (a) summer 500**  
 175 **hPa geopotential height; (b) sea-level pressure in summer; (c)-(d) the same variables but in winter.**

176

177 **3.2 Seasonal variations of LLJs**

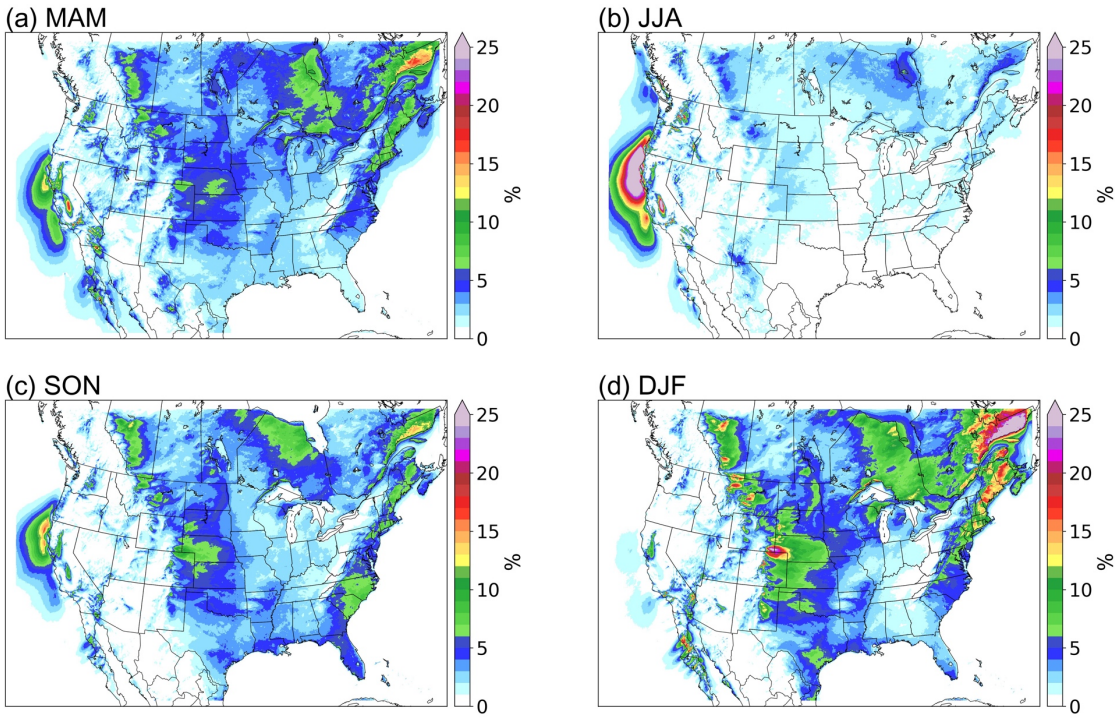
178 **3.2.1 Northerly LLJs**

179 Figure 3 illustrates the seasonal frequency distribution of Northern Low-Level Jets (N-LLJs). The frequency is defined  
 180 as the ratio of the total number of LLJ occurrences to the total number of time steps in each season. Notably, the  
 181 California coastal LLJ peaks during the summer months (June, July, and August (JJA)), where frequencies exceed 25%  
 182 over a broad area stretching from the southern Oregon coast to central California. In these regions, frequencies above  
 183 5% can even extend into the Pacific Ocean near northern Baja California. However, transitioning from summer to  
 184 autumn (September, October, and November (SON)), there is a sharp decline in the frequency of this LLJ, dropping  
 185 to only 5%-15% within the core region, predominantly along the northern California coast. In winter (December,  
 186 January, and February (DJF)), occurrences are sparse, at approximately 1%-2%.

187 Conversely, various N-LLJ phenomena are more prevalent during the colder seasons. These jets primarily occur near  
 188 the eastern slopes of significant terrains such as the Rocky Mountains, Appalachian Mountains, and the Quebec



189 Labrador Plateau. High frequencies (>10%) are observed from western Alberta to Oklahoma during winter, with hot  
 190 spots sporadically located in Alberta, Montana, Wyoming, and Colorado, where frequencies reach about 20%,  
 191 particularly between Colorado and Wyoming. In more than 25% of the wind profiles analyzed, N-LLJs were  
 192 identifiable. Along the Eastern US coast, N-LLJs predominantly stretch from Maine to South Carolina with peak  
 193 frequencies of approximately 15%-20%. In eastern Quebec, N-LLJs are most frequent in winter, exceeding 25%. The  
 194 simulation also detects the presence of N-LLJ in about 10% of the time steps over Hudson Bay. Notably, the  
 195 frequencies of all aforementioned N-LLJs significantly diminish in spring, becoming scarcely detectable in summer  
 196 with frequencies mostly under 5%.



197  
 198 **Figure 3. Seasonal occurrence frequency of N-LLJs.** Frequency shown here is calculated by counting the number of  
 199 occurrences of LLJs in each three-hourly time step and then dividing the total number of LLJs in each season by the number  
 200 of time steps in that season.

201 **3.2.2 Southerly LLJs**

202 As to the patterns of S-LLJs in different seasons (see Figure 4), during winter, frequencies exceeding 10% are observed  
 203 across a vast area spanning from south Texas and the western Gulf of Mexico to southern Iowa, depicted as a deep  
 204 green area in Figure 4d. The greatest frequencies of S-LLJs (>20%) are found along the border between northeastern

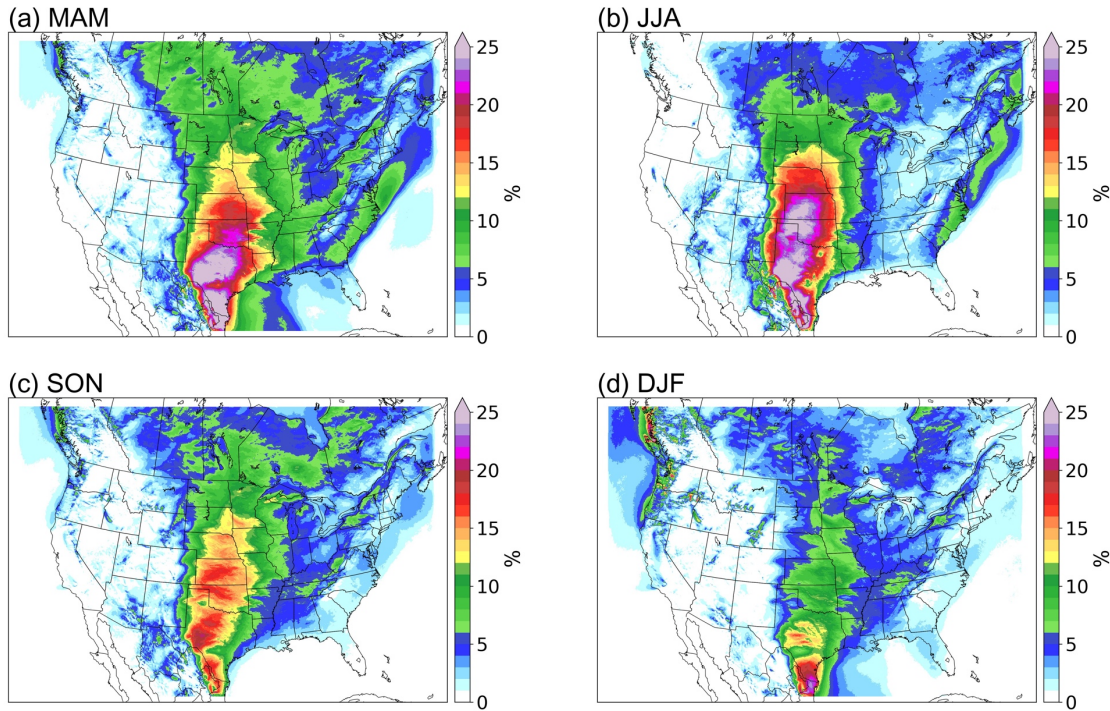
---

205 Mexico and the United States. In addition, about 15% of the simulated wind profiles in south-central Texas are  
206 identified as S-LLJs (red clusters). In the spring (March, April, and May), the frequency expands significantly in >10%  
207 of areas, with clear S-LLJ distributions detected in Manitoba, Saskatchewan, and other parts of Canada. The highest  
208 frequencies are still found in the Texas-Mexico area, where the magnitude of these frequencies increases to over 25%.  
209 This region (colored purple) also extends northward to occupy most of Texas. In winter, S-LLJs with occurrence  
210 frequencies of above 15% extend to near Colorado and Nebraska.

211 By summer, the area with frequencies greater than 10% no longer reaches to the central Canadian prairie provinces.  
212 The S-LLJs over the western Gulf of Mexico become nearly indiscernible in modeled data, with frequencies  
213 approaching 0%. Conversely, the area with frequencies exceeding 25% expands northward and is segmented into three  
214 distinct parts: along the northeast Mexico-Texas border, west-central Texas, and the central US Great Plains (western  
215 Oklahoma and southern Kansas). Regions where over 15% of wind profiles are identified as S-LLJs also spread from  
216 Colorado to near South Dakota.

217 In the fall, the magnitude of the frequency of S-LLJs decreases dramatically in the central US Plains and Texas. The  
218 frequency still maintains a level greater than 15% in most areas, but with a maximum frequency of only 20% and  
219 sporadically located in southwest Texas. The frequencies greater than 10% again expand northward and eastward in  
220 this season, reaching Manitoba and Ontario.

221 Additionally, several smaller-scale S-LLJs are evident on the seasonal S-LLJ distribution map. In spring, a narrow  
222 region of S-LLJs with a frequency greater than 5% along the eastern side of the Appalachians extends from Georgia  
223 through the western Atlantic to southern Nova Scotia. Near eastern Maryland over the Atlantic, the frequency of S-  
224 LLJs can exceed 10%. This narrow frequency belt persists through summer with the same coverage, though the  
225 frequency magnitude diminishes, and the presence of frequencies greater than 10% is no longer visible. In winter, a  
226 region where S-LLJ frequency exceeds 5% stretches from southwest Oregon to the west coast of British Columbia,  
227 Canada. However, by spring, S-LLJs with frequencies above 5% occur solely over the ocean west of British Columbia,  
228 and in summer, S-LLJs are virtually undetectable in this region.



229

230 **Figure 4. Seasonal frequency of S-LLJs.**

231 To summarize, for the LLJ systems that have been investigated by many researchers, the convection-permitting WRF  
 232 model performs well in observing the Great Plains S-LLJ and California coastal N-LLJ during the summer. But as to  
 233 the winter LLJs that lack attention, it is essential to compare and validate the occurrence and features revealed by  
 234 WRF simulation. Therefore, the ERA5 reanalysis dataset is applied in this study for capturing the LLJs in winter using  
 235 the same criterion. Appendix after the text shows the results of the comparison between ERA5 and WRF simulation.

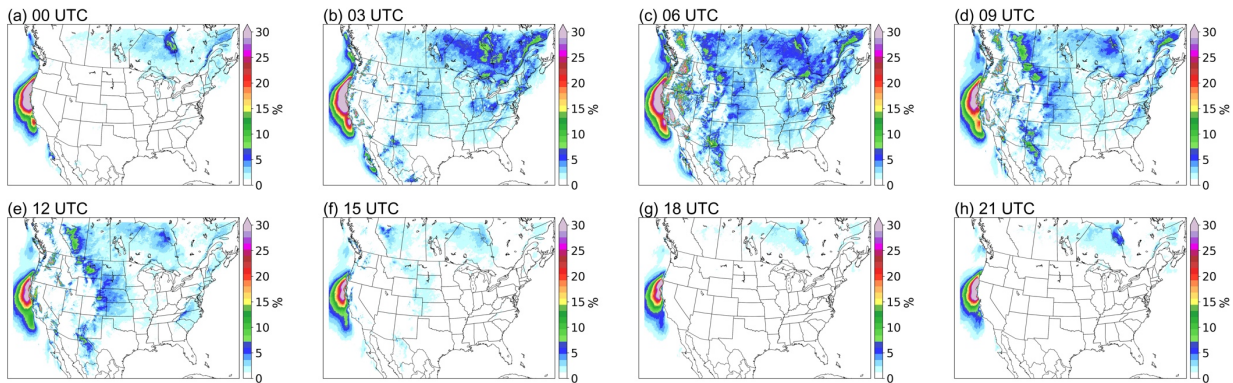
236 **3.3 Diurnal variations of LLJs**

237 To show the diurnal features of the LLJs, we selected summer and winter as the representative seasons because S-  
 238 LLJs and N-LLJs occur most frequently in these seasons, respectively. Below, the descriptions are divided into N-  
 239 LLJs and S-LLJs.

240 **3.3.1 Northerly LLJs**

241 The California coastal N-LLJ is the most highlighted low-level jet system in this region in summer. As seen in Figure  
 242 5, it occurs throughout the day over the eastern Pacific Ocean from Oregon to the California coast. Figure 5 also shows  
 243 that the California Coastal N-LLJ has diurnal characteristics: from 21 UTC (1 pm LST in California), the low-level

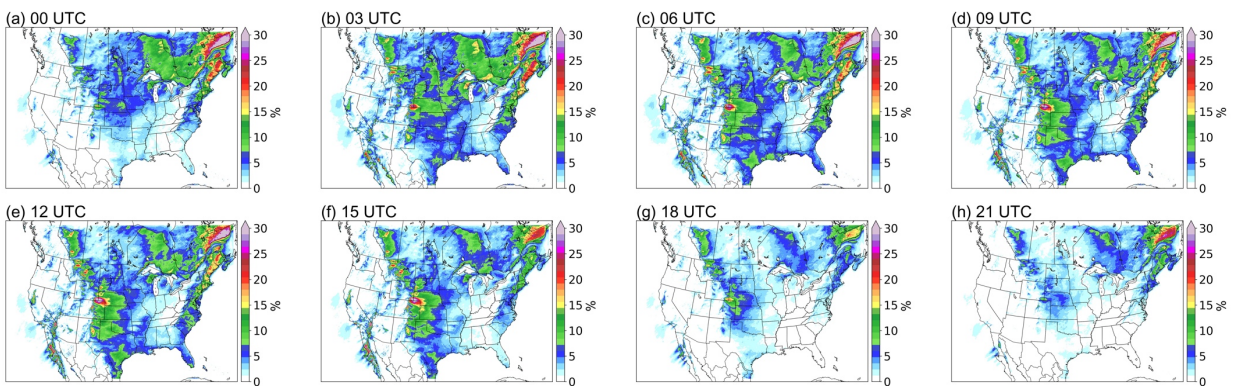
244 jet begins to develop, with a N-LLJ frequency of >30%, expanding until it reaches its maximum at 03 UTC – 06 UTC.  
 245 Then the high-frequency coverage of the California coastal LLJ gradually shrinks, reaching the minimum at 18 UTC  
 246 and only existing off the northwest coast of California.



247

248 **Figure 5. Diurnal frequency of N-LLJs in the summer (JJA).**

249 In winter (Figure 6), three types of N-LLJs over the Hudson Bay Lowlands, the eastern slopes of the Quebec Labrador  
 250 Plateau, and the Appalachians display similar diurnal fluctuations. All three N-LLJs reach their highest frequency at  
 251 03 UTC (10 pm EST) and their lowest at 18 UTC (1 pm EST). The only difference among the three types is that the  
 252 smallest frequency of the Quebec N-LLJ still endures at a level of greater than 15%, while the other two N-LLJs  
 253 mostly have frequencies of about 5%. The smallest frequency (~5%) of N-LLJs occurs downstream of the Rocky  
 254 Mountains (over Alberta, Montana, and Kansas) at 21 UTC. In the subsequent development stage, the changes in the  
 255 sporadic hot spots distributed near the eastern boundary of the Rocky Mountains are more significant. As seen in  
 256 Figure 6, frequency starts growing from 00 UTC and then peaks at 12 UTC, especially the wind maxima located in  
 257 Colorado, Wyoming, and Kansas, where the highest frequency can be >25%.

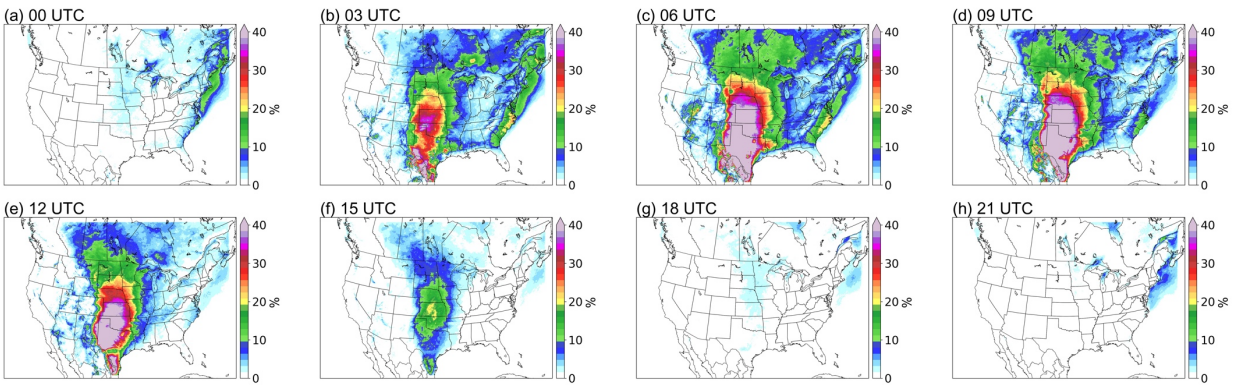


258

259 **Figure 6. Diurnal frequency of N-LLJs in winter (DJF).**

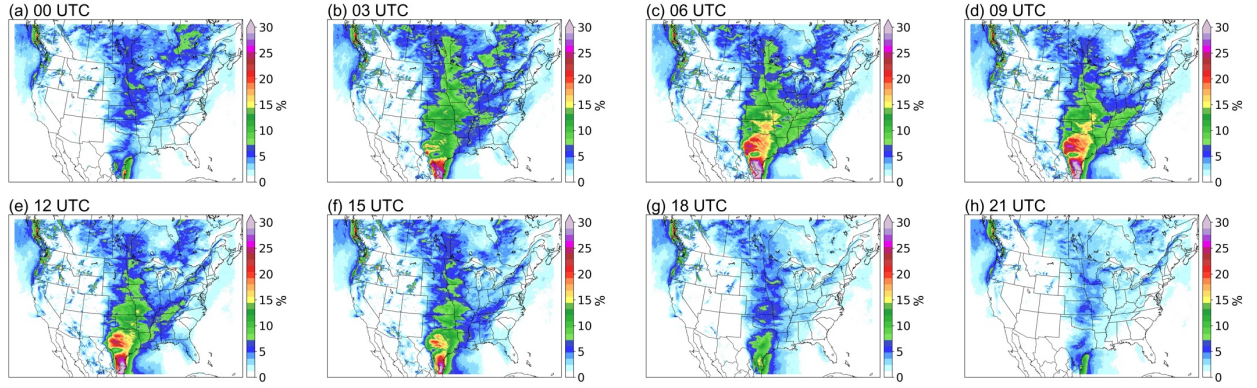
260 **3.3.2 Southerly LLJs**

261 In summer, the Great Plains S-LLJ occurs more frequently than in other seasons, and its diurnal variability is also the  
262 strongest in this season (see Figure 7). At noon local time and in the afternoon (18 UTC – 00 UTC, 12-18 CST), almost  
263 no S-LLJs occur over the central US (frequency <5% or about 0%). In contrast, the Great Plains LLJ begins to develop  
264 at 03 UTC, when a frequency of over 25% extends from Mexico to Kansas. It reaches maximum strength at midnight  
265 (06 UTC – 09 UTC, 00 – 03 CST), when the frequency reaches over 30% and the high-frequency coverage enlarges  
266 to the Dakotas, the border of the eastern Rocky Mountains, and western Minnesota, Missouri, and Louisiana. Summer  
267 S-LLJs are also active in southern Canada at night and in the early morning. In Saskatchewan, Manitoba, and central  
268 Ontario (03 UTC – 12 UTC, as shown in Figure 7), S-LLJs are found with frequency >15%. In the eastern US and  
269 Atlantic, S-LLJs occur most frequently at midnight (03 UTC – 06 UTC).



270  
271 **Figure 7. Diurnal frequency of S-LLJs in summer (JJA).**

272 For the cold season (Figure 8), even though the Great Plains LLJ is the most inactive based on the description in  
273 section 3.2, it still has a clear diurnal variation. Compared with the results in summer, the diurnal cycle of Great Plains  
274 LLJ in winter is not that pronounced: It mainly occurs over the western Gulf of Mexico and southern Texas, with the  
275 frequency in the afternoon (18 UTC – 21 UTC) declining to 5-10%. The S-LLJ develops from 03 UTC, gradually  
276 generating two high-frequency (20%-25%) centers in mid- and southeastern Texas at 06 UTC – 12 UTC. As for the  
277 S-LLJ near Vancouver Island, it is hard to see the diurnal variability: There is only a slight magnitude growth of  
278 frequency from the afternoon (00 UTC) to the evening (06 UTC), and the coverage is almost the same.



279

280 **Figure 8. Diurnal frequency of S-LLJs in winter (DJF).**

281

#### 282 4 Formation and evolution mechanisms of various LLJs

283 Section 3's results illustrate the occurrence frequency of LLJs over North America, particularly their seasonal and  
 284 diurnal features. To explain the mechanisms, the inertial oscillation theory from Blackadar (1957) is used. Using this  
 285 theory, we start from the horizontal momentum equations and divide the actual horizontal wind  $u/v$  into two  
 286 components—geostrophic wind  $u_g/v_g$  and ageostrophic wind  $u_a/v_a$ :

$$287 \quad \frac{d(u_g + u_a)}{dt} = -\frac{1}{\rho} \frac{\partial P}{\partial x} + f(v_g + v_a) \quad (1.1)$$

$$288 \quad \frac{d(v_g + v_a)}{dt} = -\frac{1}{\rho} \frac{\partial P}{\partial y} - f(u_g + u_a) \quad (1.2)$$

289

290 In which  $\rho$  is air density,  $P$  is pressure, and  $f$  is the Coriolis parameter. Assuming the horizontal pressure gradient is

291 fixed, the geostrophic wind is a constant as well, which means  $\frac{du_g}{dt} = \frac{dv_g}{dt} = 0$ :

$$292 \quad \frac{du_a}{dt} = -\frac{1}{\rho} \frac{\partial P}{\partial x} + f(v_g + v_a) \quad (2.2)$$

$$293 \quad \frac{dv_a}{dt} = -\frac{1}{\rho} \frac{\partial P}{\partial y} - f(u_g + u_a) \quad (2.2)$$

294

295 When the definition of geostrophic wind  $u_g = -\frac{1}{\rho f} \frac{\partial P}{\partial y}$  and  $v_g = \frac{1}{\rho f} \frac{\partial P}{\partial x}$  is combined, the equation (2) is:

$$296 \quad \frac{du_a}{dt} = f v_a \quad (3.1)$$

$$297 \quad \frac{dv_a}{dt} = -f u_a \quad (3.2)$$

298

299 If  $\frac{d}{dt}$  is taken to both sides of the equations (3), then we get  $\frac{d^2 u_a}{dt^2} = -f^2 u_a$ , and  $\frac{d^2 v_a}{dt^2} = -f^2 v_a$ , thereby:

300 
$$u_a = c_1 \cos(ft) + c_2 \sin(ft) \quad (4.1)$$

301 
$$v_a = c_2 \cos(ft) - c_1 \sin(ft) \quad (4.2)$$

302

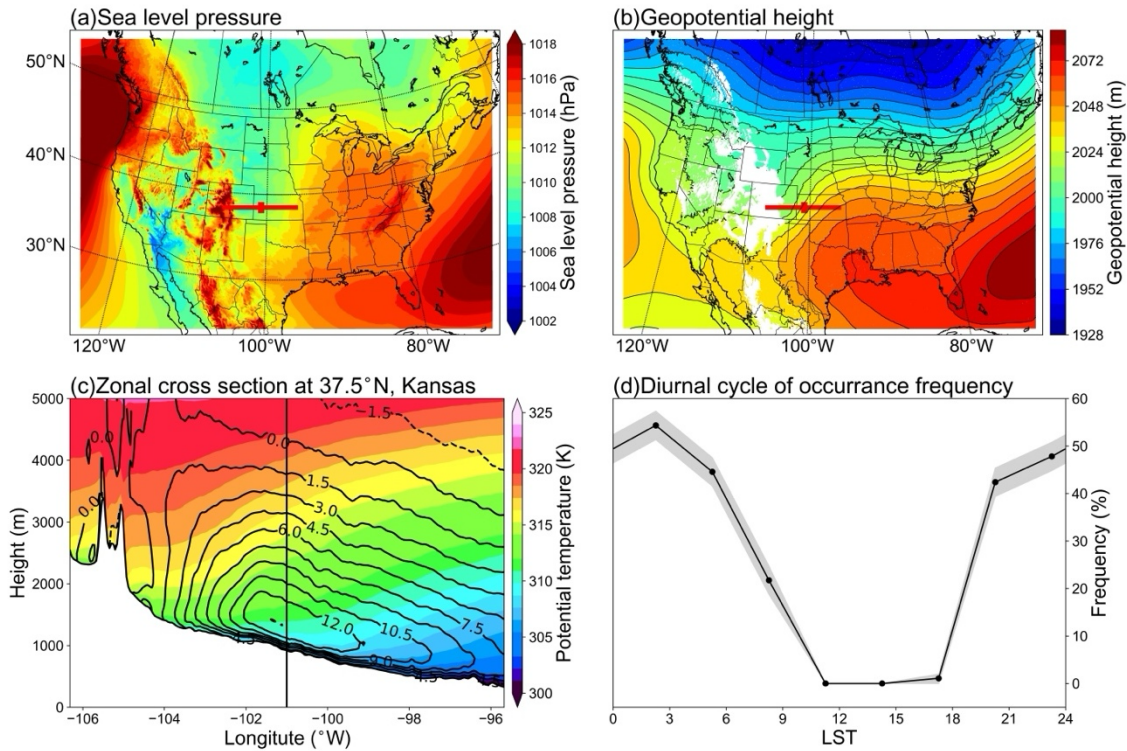
303 Therefore, according to the equations (4), the ageostrophic wind should theoretically have a circle-pattern variation  
304 and the vector must rotate clockwise with a period of  $2\pi/f$  (Blackadar, 1957; Van de Wiel et al., 2010). Under the  
305 condition of a constant geostrophic wind—when the ageostrophic vector rotates from the opposite to the same  
306 direction of geostrophic wind—the wind transitions from subgeostrophic to supergeostrophic. This change occurs  
307 because of decoupling with surface friction effects, then the wind gets unbalanced.

308 Other theories also help explain the formation of LLJs, such as the sloping-terrain thermodynamic mechanism (Holton,  
309 1967) and background synoptic system forcing (Uccellini et al., 1987). To understand the characteristics of the LLJs  
310 in this study, three typical cases are analyzed: Great Plains S-LLJ, Quebec N-LLJ, and California coastal N-LLJ. The  
311 locations for extracting data are shown in Figure 1 (solid lines and stars a, b, c).

#### 312 **4.1 Great Plains S-LLJ**

313 As Section 3's results show (see Fig. 7), the Great Plains S-LLJ typically occurs in summer and more frequently at  
314 night. To investigate its associated meteorological condition, this study extracts all the Great Plains S-LLJ cases occurs  
315 at the jet core in JJA. The jet core is defined by where the mean meridional wind is the strongest on the cross-section,  
316 and it locates at star A (shown in figure 1). The mean sea-level pressure and 800 hPa geopotential height are shown  
317 in Figure 9a and 9b, respectively. The background large-scale circulations indicate that, at all the time points when  
318 the Great Plains S-LLJ occurs, the range of the subtropical anticyclone extends east of the Great Plains at both ground  
319 and low-level atmosphere. A high-pressure ridge is located near the gulf coast of Mexico and Texas (Figure 9b). Thus,  
320 clearly, the zonal pressure/geopotential gradient in the central US guides the dominant southerly winds around this  
321 region. The cross-section in Figure 9c illustrates a strong baroclinicity and shows that the isentropic line incline moves  
322 from east to west, as is typical for the sloping-terrain heating effect (Holton, 1967). This effect generates an upslope  
323 wind on the east side of the slope, and the airstream gradually turns northward due to the Coriolis force, creating the  
324 southerly LLJs. On the other hand, as can be seen in the frequency cycle in Figure 9d, at noon local time (at the

325 selected point-a in Figure 1), the frequency of the Great Plains LLJ is very low (close to 0%), rising to more than 40%  
 326 after 18 LST even if the radiation is not at the day's peak.



327  
 328 **Figure 9. Background circulations of the Great Plains S-LLJ in JJA: (a) sea-level pressure, (b) geopotential height of 800**  
 329 **hPa, (c) cross section including meridional winds (lines) and potential temperature (shading), and (d) diurnal cycle of**  
 330 **frequency, with the shaded 95% confidence intervals. The red lines and points in (a) and (b) show the position of cross-**  
 331 **section and chosen jet core, the vertical line in (c) shows the zonal location of the chosen jet core.**

332 To explain the nighttime enhancement of S-LLJ, we analyzed the wind vectors using inertial oscillation theory. To  
 333 show more significant diurnal variation, all the time points, including the LLJs that did not occur, were considered.  
 334 Figure 10a is the hodograph of jet-core winds at point-a near the Great Plains, and their temporal mean is computed  
 335 at 3-hourly intervals in summer. It is noted here that the “jet-core” means the position where LLJ occurs horizontally  
 336 the most frequently on the cross-section. Compared with the mean actual wind (blue arrow), the deviation at each  
 337 local time shows a clear clockwise rotation. The wind speed begins increasing after 17 LST. Nevertheless, the analysis  
 338 for Figure 9 indicates the sloping heating effect, meaning that the geostrophic wind is not fixed.

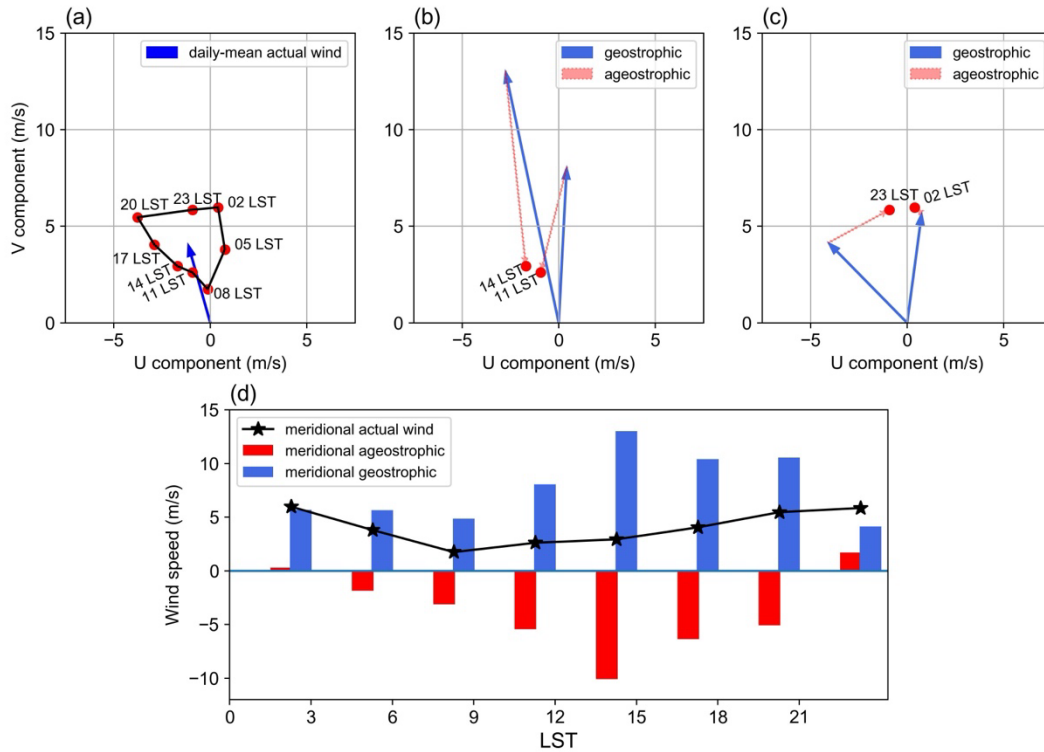
339 Thus, to obtain the ageostrophic winds, we computed the geostrophic components by pressure gradient and subtracted  
 340 them from the actual airflow. According to the aforementioned definition of geostrophic wind,  $u_g$  and  $v_g$  are



---

341 calculated by the horizontal pressure gradient  $\frac{\partial P}{\partial y}$  and  $\frac{\partial P}{\partial x}$ , respectively. By choosing four grids surrounding point-a, we  
342 first interpolated the pressure value to the same level as the LLJ core height. Then, we adopted the central difference  
343 equation  $\frac{\Delta P}{\Delta x} = \frac{P_{i+1} - P_{i-1}}{x_{i+1} - x_{i-1}}$  or  $\frac{\Delta P}{\Delta y} = \frac{P_{i+1} - P_{i-1}}{y_{i+1} - y_{i-1}}$  to obtain the pressure gradients at point-a, where i is the index of the grid  
344 point at point-a.

345 Figures 10b and 10c display geostrophic wind vectors (blue arrows) and ageostrophic vectors (pink) at noon and  
346 midnight. The southerly geostrophic flows are much stronger in the afternoon (10b) than at midnight. The ageostrophic  
347 winds flow mostly in the opposite direction, limiting the actual wind speed. At night (10c), the geostrophic wind  
348 direction rotates clockwise from that of the afternoon as the pressure gradient changes. Considering the relative  
349 positions of blue and pink vectors at 23 LST and 01 LST, ageostrophic flow has rotated roughly 150 degrees to  
350 enhance the geostrophic winds, thereby creating a super-geostrophic state. Although the inertial oscillation theory can  
351 help explain some aspects of wind behavior, the real situation is more complex than initially thought. Figures 10b and  
352 10c indicate that by 02 LST, the wind is almost entirely geostrophic with only negligible ageostrophic perturbations.  
353 This suggests that the diurnal changes in the geostrophic wind and pressure gradient may provide a complicating  
354 background that prevents the inertial oscillation theory from fully prevailing. While the inertial oscillation theory can  
355 provide valuable insights, it should not be relied upon as the sole explanation for LLJs at the Great Plains. Instead, a  
356 more comprehensive understanding of atmospheric dynamics is necessary to fully comprehend the behavior of the  
357 wind, particularly when dealing with diurnally changing conditions. Figure 10d compares different meridional wind  
358 components' amplitudes. The geostrophic wind contributes significantly to the southerly wind during the day, peaking  
359 at 14 LST (blue bars). The northerly ageostrophic wind (red bars) is highest during the day, indicating the strongest  
360 negative impact from friction. The meridional ageostrophic component decreases and eventually reverses at 23 LST,  
361 showing a process from sub- to super-geostrophic status. In summary, the thermodynamic circulation near the slopes  
362 of the Great Plains contributes to the strong southerly airflow, while the inertial oscillation plays a critical role in  
363 forming the nocturnal southerly LLJ.



364

365 **Figure 10. (a) Hodograph of jet-core winds for the Great Plains S-LLJ every 3 hours over the whole JJA (red dots – solid**  
 366 **line) and the daily averaged actual wind velocity (blue vector); vectors of mean jet-core geostrophic winds (solid blue) and**  
 367 **ageostrophic winds (dashed red) at (b) 11/14 LST and (c) 23/02 LST; (d) diurnal cycles of meridional components of actual**  
 368 **(black line), geostrophic (blue bars), and ageostrophic winds (red bars).**

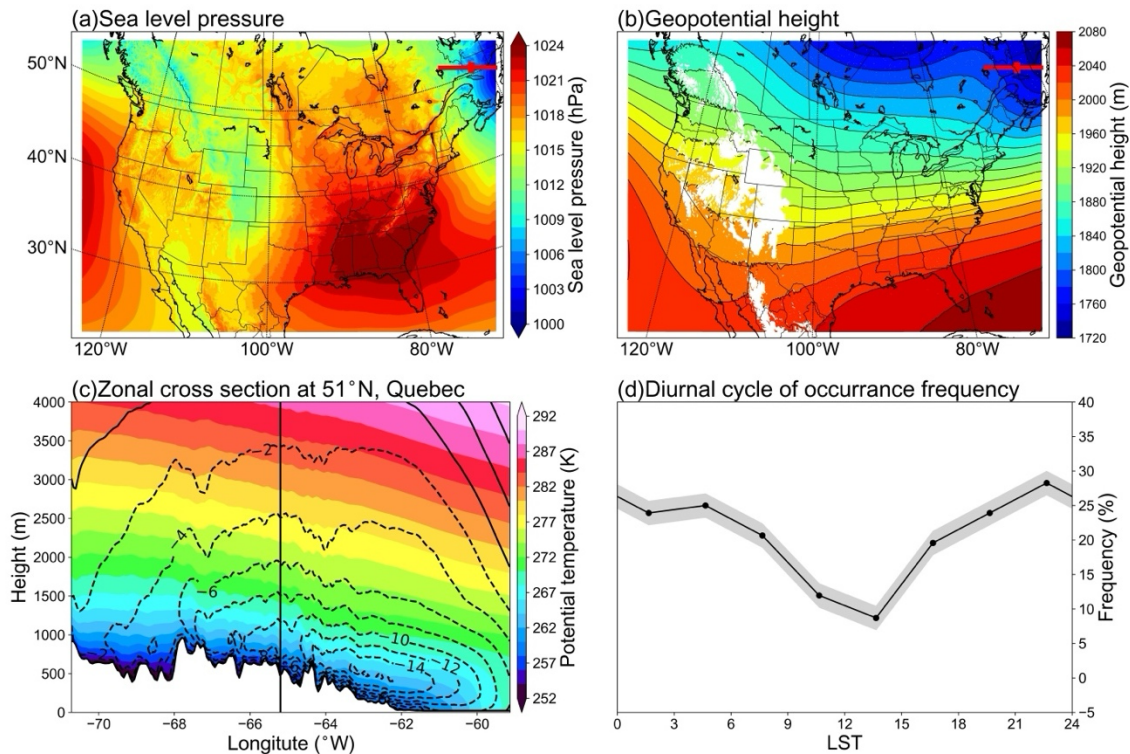
369

#### 370 4.2 Quebec N-LLJ

371 Similarly, for the Quebec N-LLJ that is typically observed in winter, we selected all the LLJ cases at point-b (see the  
 372 position in Figure 1) in DJF to generate the background circulation pattern. The background large-scale circulations  
 373 indicate that the northeastern coast of Canada lies to the west of a strong surface low-pressure system (Figure 11a),  
 374 while in the lower troposphere, a ridge on the east side of Hudson Bay occupies the Labrador Plateau (Figure 11b).  
 375 This combination brings the northerly momentum to the downstream eastern coast. In fact, the background circulation  
 376 is consistent with the shallow baroclinic structure of Quebec N-LLJ in winter, that is, the thermal difference between  
 377 relatively warm sea and cold land. The cross-section in Figure 11c shows the thermodynamic structure of this N-LLJ:  
 378 A well-defined low-level jet core is located above land and close to the coastline (approximately 63°W). With a  
 379 maximum wind speed of more than 16 m s<sup>-1</sup> and a height of about 400 m, the jet core is located above the mixed layer

380 under the warm air covering and on the land side. Notably, the steep isentropic lines slope towards the ocean and  
 381 finally sink at the position of 60°W. The onshore isentropic lines are flat and dense above the LLJ core, which means  
 382 the environment is quite stable. This is helpful to maintain the structure of the LLJ, when vertical motion is inhibited,  
 383 and horizontal wind is enhanced. Compared with the sloped isentropic lines in the Great Plain S-LLJ case (Figure 9c),  
 384 the stability over Great Plain is not as high as in this case, so this difference in stability helps explain the variation in  
 385 wind speeds between these two cases.

386 In addition, the diurnal cycle of frequency (Figure 11d) shows that the diurnal signal and peak frequency of Quebec  
 387 N-LLJ are much weaker than the Great Plains S-LLJ, becoming weakest at noon and peaking at midnight, which is  
 388 consistent with the results reported in Section 3. This diurnal variation can be explained by the baroclinicity near this  
 389 region: At night in winter, the land temperature drops faster than the ocean temperature due to radiative cooling,  
 390 enhancing the land-sea contrast and thereby the thermal wind above. The gentle slope on the east of the Labrador  
 391 Plateau could generate the slope heating effect in the daytime. In this way, the related temperature gradient from east  
 392 to west offsets the land-sea thermal difference.



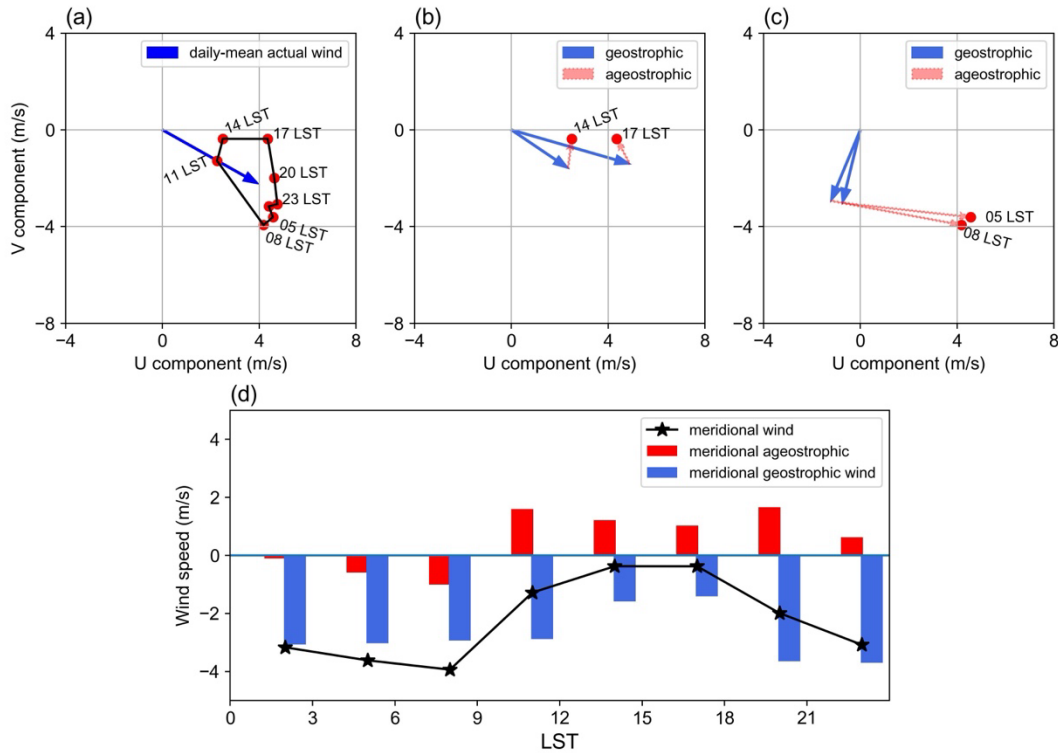
393  
 394 **Figure 11. Background circulations of the Quebec N-LLJ in DJF: (a) sea-level pressure, (b) geopotential height of 800 hPa,**  
 395 **(c) cross section including meridional winds (lines) and potential temperature (shading), and (d) diurnal cycle of frequency**

---

396 **with the shaded 95% confidence intervals. The red lines and points in (a) and (b) show the position of cross-section and**  
397 **chosen jet core, the vertical line in (c) shows the zonal location of the chose jet core.**

398 As for the impact of inertial oscillation on the Quebec N-LLJ, the hodograph of averaged 3-hourly winds extracted at  
399 point-b (Figure 12a) also illustrates a clear clockwise rotation of wind deviations compared with the daily mean (blue  
400 arrow). Figure 12b and 12c show that the geostrophic and ageostrophic wind vectors contribute to the diurnal cycle in  
401 the afternoon and morning, respectively. Even though the direction of geostrophic wind changes significantly, the  
402 relative angles between ageostrophic and geostrophic arrows indicate that the ageostrophic flow rotates clockwise.  
403 The geostrophic wind is weakened by ageostrophic wind in the afternoon (Figure 12b), whereas the supergeostrophic  
404 state is generated in the morning (Figure 12c).

405 Focusing only on the meridional amplitudes validates this characteristic. In Figure 12d, the blue line that represents  
406 the mean actual meridional wind has the same diurnal trend as the frequency variation in Figure 11d. The northerly  
407 wind is weakest in the afternoon, peaking at night and in the early morning. Similarly, the variation of meridional  
408 geostrophic flow has a consistent phase with the actual meridional wind, which is explained by the baroclinic structure  
409 near the Quebec coast mentioned above. The meridional ageostrophic wind in this region also promotes the formation  
410 of N-LLJ. The ageostrophic wind drags the geostrophic component in the afternoon, before reversing to a consistent  
411 direction with the northerly geostrophic flow at night and in the morning. This trend is also the result of decreasing  
412 friction after sunset. Therefore, the evolution of Quebec N-LLJ derives from both inertial oscillation and land-sea  
413 thermal contrast in winter.



414

415 **Figure 12. (a) Hodograph of jet-core winds for the Quebec N-LLJ every 3 hours over the whole DJF (red dots – solid line)**  
 416 **and the daily averaged actual wind velocity (blue vector); vectors of mean jet-core geostrophic winds (solid blue) and**  
 417 **ageostrophic winds (dashed red) at (b) 14/17 LST and (c) 05/08 LST; (d) diurnal cycles of meridional components of actual**  
 418 **(black line), geostrophic (blue bars), and ageostrophic winds (red bars).**

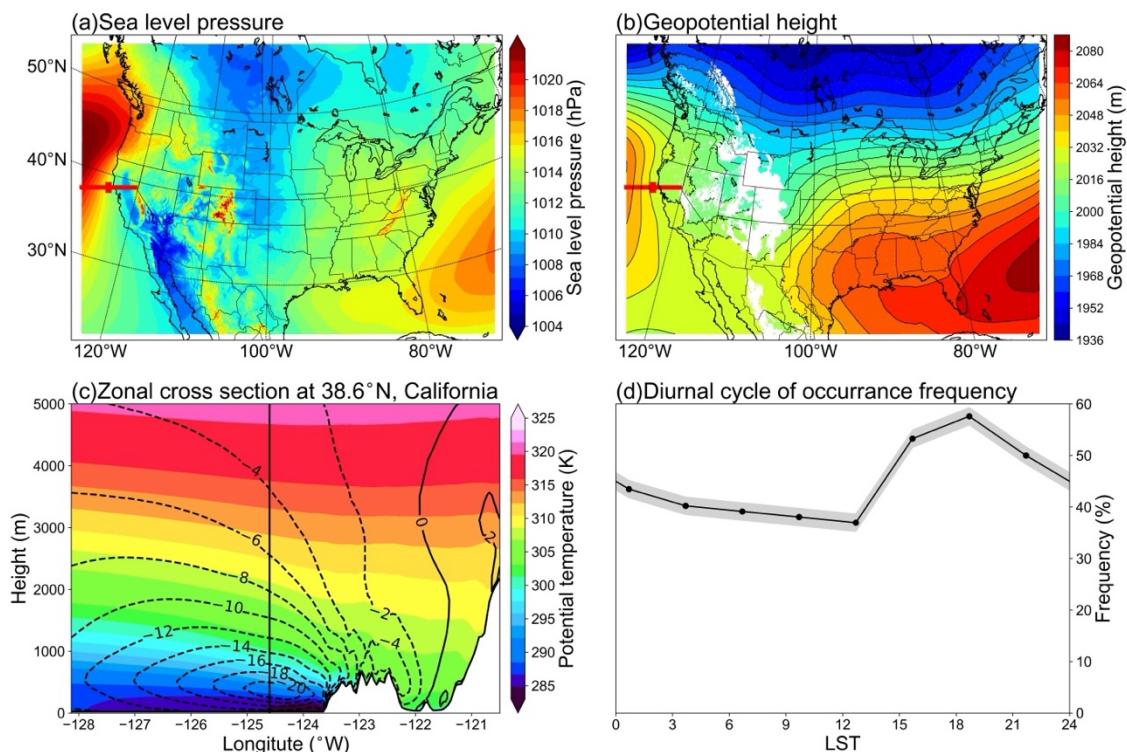
419

### 420 4.3 California coastal N-LLJ

421 The California coastal N-LLJ is similar to the one in Quebec, but it occurs more often in summer afternoons or  
 422 evenings over the ocean. Figure 13a shows that a relatively strong high-pressure system is located on the east coast of  
 423 the Pacific Ocean, trending NE-SW, although half of the structure is beyond the boundary of the domain. On the 800  
 424 hPa isobaric surface in Figure 13b, there is also an anticyclone system in the same location, whose eastern contour is  
 425 roughly parallel to the coastline, guiding the airflow to the south. Therefore, this pair is also forced by the thermal  
 426 difference between land and sea, but contrary to the LLJ in Quebec, in summer, when the California LLJ occurs  
 427 frequently, it has the characteristics of the cool sea-hot land. Figure 13b also shows that the isobars near Cape  
 428 Mendocino are relatively strong, making the ridge of high pressure extend northeastward of the Cape. This extension  
 429 is generally believed to occur due to pressure perturbation caused when northerly winds converge at this position after

430 being obstructed (Rahn and Parish, 2007). Regarding the cross-section structure shown in Figure 13c, the jet core is  
 431 located at steep isentropic lines above the ocean at a height of 500 m. On the coast of California, the LLJ is close to  
 432 the mountains. The maximum central wind speed of California coastal LLJ exceeds 20 m s<sup>-1</sup>, whereas Quebec N-  
 433 LLJ's max core wind is only about 14 m s<sup>-1</sup>. Based on baroclinicity, the isentropic lines slope towards the continent  
 434 and finally sink near the coastline.

435 The core wind speed in California's coastal LLJ is higher than that of Quebec's LLJ because the land-sea contrast is  
 436 more significant in summer than in winter and the formed sea breeze front generates flow convergence under the  
 437 blockage caused by the west coast mountains. On the other hand, the atmosphere over the sea is more stable because  
 438 the isentropic lines are flatter and denser than Quebec's case, which also favors the development of LLJ. In contrast,  
 439 the east coast of Quebec is relatively gentle, which may account for its lower wind speed. California's LLJ occurs  
 440 frequently at each time step, and its diurnal signal is weaker compared, for example, to the signal in the Great Plain  
 441 S-LLJ. As well, the California signal stays at frequency of over 35%. California's LLJ occurs most frequently at  
 442 around 18 LST and starts to decline after sunset, which is generally consistent with the coastal baroclinicity.

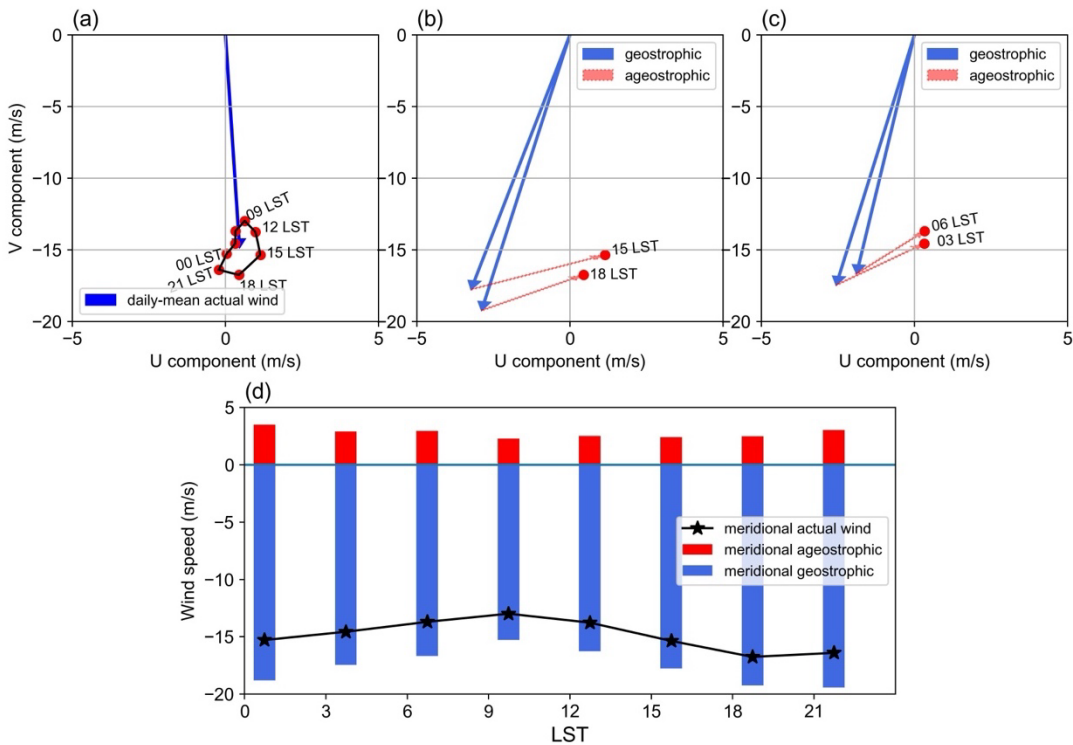


443  
 444 **Figure 13. Background circulations of the California coastal N-LLJ in JJA: (a) sea-level pressure, (b) geopotential height**  
 445 **of 800 hPa, (c) cross section including meridional winds (lines) and potential temperature (shading), and (d) diurnal cycle**

446 of frequency with the shaded 95% confidence intervals. The red lines and points in (a) and (b) show the position of cross-  
 447 section and chosen jet core, the vertical line in (c) shows the zonal location of the chosen jet core.

448

449 The wind deviations for California’s N-LLJ shown in the hodograph (Figure 14a) still have a clockwise rotation in 24  
 450 hours. However, compared with the magnitude of the daily mean jet-core wind, this diurnal cycle is not quite as  
 451 obvious as the cycle for Quebec and Great Plain LLJs, but it is similar to the frequency cycle shown in Figure 13d. In  
 452 comparison between geostrophic and ageostrophic winds (Figure. 14b and 14c), during the afternoon (15 and 18 LST),  
 453 the amplitude of geostrophic wind is the largest, and the ageostrophic flow diminishes the geostrophic wind. However,  
 454 in the morning 12 hours later, the relative angle between ageostrophic and geostrophic vectors does not change,  
 455 meaning that the ageostrophic wind is still weakening the geostrophic wind and that there is no rotation of the  
 456 ageostrophic wind, as Blackadar inertial oscillation theory describes. Figure 14d helps to explain the change in  
 457 meridional winds. Looking at the magnitudes of ageostrophic winds, one can see that all are weak and southerly and  
 458 that they do not exhibit a significant diurnal signal. Furthermore, the change of geostrophic wind is highly consistent  
 459 with the trend of the actual meridional wind. Thus, the N-LLJ in California can be considered mostly as geostrophic  
 460 and the diurnal variation as being related to the change in geostrophic winds.



---

462 **Figure 14. (a) Hodograph of jet-core winds for the California coastal N-LLJ every 3 hours over the whole JJA (red dots –**  
463 **solid line) and the daily averaged actual wind velocity (blue vector); vectors of mean jet-core geostrophic winds (solid blue)**  
464 **and ageostrophic winds (dashed red) at (b) 15/18 LST and (c) 03/06 LST; (d) diurnal cycles of meridional components of**  
465 **actual (black line), geostrophic (blue bars), and ageostrophic winds (red bars).**

466

## 467 **5 Discussion and conclusion**

468 This study applied a convection-permitting WRF model to conduct the analysis of LLJs in North America. The  
469 previous research for LLJs mainly focused on observation data, which have no fine coverage in temporal or spatial  
470 resolution. The studies using in-situ observations may ignore some important features. Despite their better coverage,  
471 reanalysis datasets usually have a coarse spatial resolution, and can introduce large inaccuracies in the identification  
472 of LLJs. In addition, the application of general numerical modeling cannot avoid the uncertainty caused by  
473 parameterizing small-scale physical processes. In contrast, high-resolution convection-permitting climate simulations  
474 can provide relatively more comprehensive descriptions of LLJs, especially for areas with complex geographic  
475 conditions or regions that lack soundings. Previous studies using high-resolution models conducted case analyses only  
476 of LLJs in a specific region (Aird et al., 2022). By expanding the target domain to the whole of North America and  
477 revealing the climatological characteristics of LLJs in different regions and scales, this paper provides an accurate  
478 reference for future research on LLJ-related processes in North America.

479 The convection-permitting WRF model is able to recapture some LLJs that have been previously studied, such as the  
480 Great Plain S-LLJ and the California coastal N-LLJ in the eastern Pacific Ocean and has obtained relatively consistent  
481 results. The results indicate that the S-LLJ in the central US Plain is the most frequent and active in warm seasons and  
482 that three critical high-frequency centers occur in summer: the northeast Mexico-Texas border, west-central Texas,  
483 and western Oklahoma to southern Kansas. This last result is consistent with the climatology generated by Doubler et  
484 al. (2015) using the NARR reanalysis data, but the patterns here are more representative of the topographic features  
485 in central and southern Texas. In addition, compared with the 40-year rawinsonde climatology in the central US by  
486 Walters et al. (2008), our study reveals that the S-LLJ frequency range of these three centers in the central US in  
487 summer is 25%-30%, which is slightly lower than the 35% reported in the 2008 study. However, given the  
488 underestimated frequencies of 15%-20% in NARR climatology, there is an advantage of using high-resolution  
489 simulations in the vertical direction. Even though the simulation period does not match the time range of the literature  
490 exactly, the characteristics transcend specific time frames still offer a reference.



---

491 The convection-permitting simulation can also capture LLJs that were poorly detected previously using coarser  
492 resolution models and observational datasets. The winter N-LLJs over the eastern Rocky Mountains described in this  
493 paper are generally distributed over the central US from the Dakotas to Oklahoma with a low frequency (>10%) and  
494 over several sporadic small areas with a high frequency (>20%) along the boundary of the Rockies. The main  
495 seasonal/diurnal variations identified in this study agree with those seen using rawinsonde data (Walters et al., 2008)  
496 and NARR reanalysis (Douber et al., 2015). But the frequency of the LLJ occurrence over Nebraska-Kansas was  
497 underestimated in both convection-permitting simulations (~10%) and NARR (~7%), while high-frequency hot spots  
498 from Alberta to Colorado were not detected in either of the above-mentioned studies, probably because measurements  
499 are lacking in these regions. The high-resolution simulation also detected LLJs on which researchers have hardly  
500 focused: N-LLJs near the eastern Quebec coast and in the Appalachians Mountains, as well as an S-LLJ over the  
501 British Columbia coast. In the work of Douber et al. (2015), these LLJs were shown in the climatology patterns, but  
502 the 4-km WRF simulation offered more detailed descriptions of their locations. For example, this study found that the  
503 Appalachian N-LLJ extends from Georgia to the northwestern Atlantic, especially on summer nights (03 UTC – 06  
504 UTC), while NARR only captured LLJ occurrences over the middle coast of the Atlantic. The maximum frequency  
505 (7-10%) detected in the NARR study is also less than what is illustrated here. As for the Quebec N-LLJ, the 4-km  
506 WRF revealed that it mostly occurs onshore near the coast with a frequency of over 25% in winter, but NARR only  
507 provided a coarse occurrence distribution over northeastern Canada.

508 Based on the inertial oscillation theory (Blackadar, 1957) and the baroclinic theory near complex terrain (Holton,  
509 1967), this paper also analyzed the background and formation mechanisms of three LLJs: the Great Plain S-LLJ,  
510 Quebec N-LLJ, and California coastal N-LLJ. Generally, all these LLJs are impacted by the thermodynamic  
511 circulations generated near their topography. The Great Plain S-LLJ is affected by slope heating, and the LLJs over  
512 Quebec and California are associated with the sea-land contrast. When the geostrophic and ageostrophic components  
513 of the LLJs are compared, results show that the inertial oscillation better explains the night enhancement of the Great  
514 Plains S-LLJ and that the diurnal feature of the Quebec N-LLJ is influenced by the combination of the Holton and  
515 Blackadar theories. As for the California coastal N-LLJ, no supergeostrophic state is found, making coastal  
516 baroclinicity variation a dominant factor for this LLJ's evolution the geostrophic wind changes.

---

517 This research adds to the existing knowledge of characteristics of the low-level wind maxima in North America, thus  
518 helping researchers obtain more reliable references about LLJs in this domain. Meanwhile, with the high-resolution  
519 features, it can provide more robust explanations for other interdisciplinary fields. The research also advances  
520 knowledge about the formation of three dominant LLJs. Although the 13-year simulation is likely too short to provide  
521 an ideal long-term climatic analysis, it is a less expensive option for finer numerical modelling in large domains.  
522 Additionally, we acknowledge certain limitations in the convection-permitting WRF simulation. While the vertical  
523 resolution in the boundary layer of this simulation is enhanced compared to other RCMs or reanalysis datasets, it  
524 remains inferior to the observation density of radiosonde soundings. Consequently, the underestimation of LLJ events  
525 in this paper is expected, as noted in previous comparative analyses. Furthermore, numerical models inherently possess  
526 biases and uncertainties. Although employing the convection-permitting scale mitigates some uncertainties, it is  
527 important to recognize the limitations of these results. Additionally, the version of the input dataset used in this  
528 research is obsolete. However, with future advancements in technology, it is expected that longer and more accurate  
529 high-resolution simulations, as well as newer input data like ERA5, will become available. Future work will address  
530 the features and formation mechanisms of the small-scale low-level wind maxima, which have yet to be investigated.

---

531 **Acknowledgments**

532 All authors thank the support of the Global Water Futures Program by the Canada First Research Excellence and the  
533 NSERC Discovery Grant.

534

535 **Data Availability Statement**

536 The WRF simulation over CONUS can be accessed at Research Data Archive of NCAR  
537 <https://rda.ucar.edu/datasets/ds612.0/>.

538

539 **Author contribution**

540 Xiao Ma: Conceptualization; data curation; formal analysis; investigation; methodology; visualization; writing-  
541 original draft.

542 Yanping Li: Conceptualization; funding acquisition; investigation; methodology; project administration; supervision;  
543 validation; writing-review and editing.

544 Zhenhua Li: Data curation; methodology; validation; visualization; writing-review and editing.

545 Fei Huo: Data curation; methodology; validation; visualization; writing-review and editing.

546

547 **Competing interests**

548 All authors disclosed no relevant relationships.

549

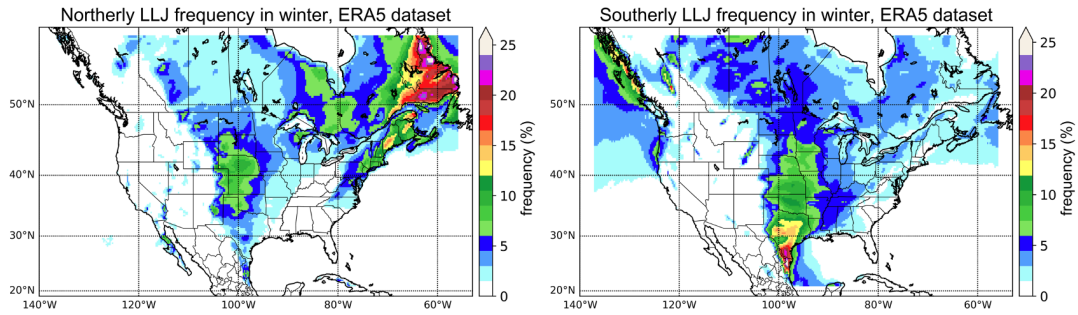
---

550 **Appendix**

551 **Winter LLJs captured by ERA5 Dataset**

552 The convection-permitting WRF simulation exhibited excellent performance in investigating well-known LLJ systems,  
553 such as the California coastal N-LLJ and the Great Plains S-LLJ. Moreover, this appendix validates WRF-simulated  
554 significant winter jet systems over North America using the ERA5 reanalysis dataset. ERA5 is a global atmospheric  
555 reanalysis dataset produced by the European Centre for Medium-Range Weather Forecasts (ECMWF). It provides  
556 hourly data on a horizontal grid space of approximately 31 km, and the time range covers from 1979 till the present.  
557 ERA5 data is widely used in climate research, weather forecasting, and various applications that require high-quality  
558 atmospheric data.

559 The validation period is the same as the WRF simulation (2000-2013). From the Figure A1 below, it is evident that  
560 during winter, a greater number of significant N-LLJ systems in the North American continent are mostly concentrated  
561 in eastern Canada. In most parts of Newfoundland and southeastern Quebec, the occurrence frequency of N-LLJs  
562 exceeds 15%, and the maximum can even surpass 25%. However, in the WRF simulation (Figure 3d), the model can  
563 only capture N-LLJs on the north bank of the St. Lawrence River due to the northern boundary of the study domain  
564 overlapping with the Quebec border. In comparison, the WRF-simulated frequency of N-LLJs in southeastern Quebec  
565 essentially exceeds 25%, overestimated by about 5% compared to the ERA5 reanalysis. Additionally, it is worth noting  
566 that the N-LLJs along the downstream of Rockies are also identified in the ERA5 dataset. The areas where the  
567 frequency exceeds 5% are mainly distributed from Alberta to northern Texas, consistent with the findings in Section  
568 3.2.1. Moreover, the high-value center (>10%) is located in central Kansas. In terms of the differences between the  
569 two datasets, the results of the WRF simulation match more geographical features and reveal scattered high-value  
570 spots (>15%) in some regions with special terrains (see Figure 3d). Furthermore, the winter Great Plains S-LLJs in  
571 ERA5 reanalysis exhibit similar features, with frequencies ranging from around 15% to 20% in southern Texas. In  
572 summary, the WRF model can accurately capture the features of winter LLJ systems, which are validated by the ERA5  
573 reanalysis dataset over northern America. Even though the frequency of LLJs occurrence is overestimated, the  
574 convection-permitting WRF simulation can provide detailed descriptions of LLJs near complex terrains.



575

576 **Figure A1. Winter occurrence frequency of N-LLJs (left) and S-LLJs (right).**

577

578

579

580 **Data Availability Statement**

581 The ERA5 dataset is available on the Copernicus Climate Change Service Information website.

582 <https://cds.climate.copernicus.eu/#!/home>

583

584

---

585 **References**

- 586 Aird, J. A., Barthelmie, R. J., Shepherd, T. J. and Pryor, S. C.: Occurrence of Low-Level Jets over the Eastern U.S.  
587 Coastal Zone at Heights Relevant to Wind Energy, *Energies*, 15(2), 445, doi:10.3390/en15020445, 2022.
- 588 Blackadar, A. K.: Boundary Layer Wind Maxima and Their Significance for the Growth of Nocturnal Inversions,  
589 *Bulletin of the American Meteorological Society*, 38(5), 283–290, doi:10.1175/1520-0477-38.5.283, 1957.
- 590 Bonner, W. D.: CLIMATOLOGY OF THE LOW LEVEL JET, *Monthly Weather Review*, 96(12), 833–850,  
591 doi:10.1175/1520-0493(1968)096<0833:cotllj>2.0.co;2, 1968.
- 592 Chen, G. T.-J., Wang, C.-C. and Lin, D. T.-W.: Characteristics of Low-Level Jets over Northern Taiwan in Mei-Yu  
593 Season and Their Relationship to Heavy Rain Events, *Monthly Weather Review*, 133(1), 20–43, doi:10.1175/mwr-  
594 2813.1, 2005.
- 595 Doubler, D. L., Winkler, J. A., Bian, X., Walters, C. K. and Zhong, S.: An NARR-Derived Climatology of Southerly  
596 and Northerly Low-Level Jets over North America and Coastal Environs, *Journal of Applied Meteorology and*  
597 *Climatology*, 54(7), 1596–1619, doi:10.1175/jamc-d-14-0311.1, 2015.
- 598 Du, Y. and Chen, G.: Heavy Rainfall Associated with Double Low-Level Jets over Southern China. Part II: Convection  
599 Initiation, *Monthly Weather Review*, 147(2), 543–565, doi:10.1175/mwr-d-18-0102.1, 2019.
- 600 Frisch, A. S., Orr, B. W. and Martner, B. E.: Doppler Radar Observations of the Development of a Boundary-Layer  
601 Nocturnal Jet, *Monthly Weather Review*, 120(1), 3–16, doi:10.1175/1520-  
602 0493(1992)120<0003:drootd>2.0.co;2, 1992.
- 603 Fu, P., Zhu, K., Zhao, K., Zhou, B. and Xue, M.: Role of the nocturnal low-level jet in the formation of the morning  
604 precipitation peak over the Dabie Mountains, *Advances in Atmospheric Sciences*, 36(1), 15–28, doi:10.1007/s00376-  
605 018-8095-5, 2018.
- 606 Gadde, S. N. and Stevens, R. J. A. M.: Effect of low-level jet height on wind farm performance, *Journal of Renewable*  
607 *and Sustainable Energy*, 13(1), 013305, doi:10.1063/5.0026232, 2021.

---

608 Hodges, D. and Pu, Z.: Characteristics and Variations of Low-Level Jets and Environmental Factors Associated with  
609 Summer Precipitation Extremes over the Great Plains, *Journal of Climate*, 32(16), 5123–5144, doi:10.1175/jcli-d-18-  
610 0553.1, 2019.

611 Hoffmann, L. and Spang, R.: An assessment of tropopause characteristics of the ERA5 and era-interim meteorological  
612 reanalyses, *Atmospheric Chemistry and Physics*, 22(6), 4019–4046, doi:10.5194/acp-22-4019-2022, 2022.

613 Holton, J. R.: The diurnal boundary layer wind oscillation above sloping terrain, *Tellus*, 19(2), 199–205,  
614 doi:10.1111/j.2153-3490.1967.tb01473.x, 1967.

615 Hong, S.-Y., Noh, Y. and Dudhia, J.: A New Vertical Diffusion Package with an Explicit Treatment of Entrainment  
616 Processes, *Monthly Weather Review*, 134(9), 2318–2341, doi:10.1175/mwr3199.1, 2006.

617 Hu, X.-M., Klein, P. M., Xue, M., Lundquist, J. K., Zhang, F. and Qi, Y.: Impact of Low-Level Jets on the Nocturnal  
618 Urban Heat Island Intensity in Oklahoma City, *Journal of Applied Meteorology and Climatology*, 52(8), 1779–1802,  
619 doi:10.1175/jamc-d-12-0256.1, 2013.

620 Iacono, M. J., Delamere, J. S., Mlawer, E. J., Shephard, M. W., Clough, S. A. and Collins, W. D.: Radiative forcing  
621 by long-lived greenhouse gases: Calculations with the AER radiative transfer models, *Journal of Geophysical*  
622 *Research*, 113(D13), doi:10.1029/2008jd009944, 2008.

623 Jain, P. and Flannigan, M.: The relationship between the Polar Jet Stream and extreme wildfire events in North  
624 America, *Journal of Climate*, 1–59, doi:10.1175/jcli-d-20-0863.1, 2021.

625 Jiménez-Sánchez, G., Markowski, P. M., Jewtoukoff, V., Young, G. S. and Stensrud, D. J.: The Orinoco Low-Level  
626 Jet: An Investigation of Its Characteristics and Evolution Using the WRF Model, *Journal of Geophysical Research:*  
627 *Atmospheres*, 124(20), 10696–10711, doi:10.1029/2019jd030934, 2019.

628 Kurkute, S., Li, Z., Li, Y. and Huo, F.: Assessment and projection of the water budget over Western Canada using  
629 convection-permitting weather research and forecasting simulations, *Hydrology and Earth System Sciences*, 24(7),  
630 3677–3697, doi:10.5194/hess-24-3677-2020, 2020.

---

631 Li, Y., Li, Z., Zhang, Z., Chen, L., Kurkute, S., Scaff, L. and Pan, X.: High-resolution regional climate modeling and  
632 projection over Western Canada using a weather research forecasting model with a pseudo-global warming approach,  
633 *Hydrology and Earth System Sciences*, 23(11), 4635–4659, doi:10.5194/hess-23-4635-2019, 2019.

634 Lin, Y., Wang, C., Yan, J., Li, J. and He, S.: Observation and simulation of low-level jet impacts on 3D urban heat  
635 islands in Beijing: A case study, *Journal of the Atmospheric Sciences*, 79(8), 2059–2073, doi:10.1175/jas-d-21-0245.1,  
636 2022.

637 Liu, C., Ikeda, K., Rasmussen, R., Barlage, M., Newman, A. J., Prein, A. F., Chen, F., Chen, L., Clark, M., Dai, A.,  
638 Dudhia, J., Eidhammer, T., Gochis, D., Gutmann, E., Kurkute, S., Li, Y., Thompson, G. and Yates, D.: Continental-  
639 scale convection-permitting modeling of the current and future climate of North America, *Climate Dynamics*, 49(1–  
640 2), 71–95, doi:10.1007/s00382-016-3327-9, 2016.

641 Ma, X., Li, Y. and Li, Z.: The projection of Canadian wind energy potential in future scenarios using a convection-  
642 permitting regional climate model, *Energy Reports*, 8, 7176–7187, doi:10.1016/j.egy.2022.05.122, 2022.

643 Miao, Y., Guo, J., Liu, S., Wei, W., Zhang, G., Lin, Y., Zhai, P., Zhai, P., Lin, Y., Zhang, G., Wei, W., Liu, S., Guo,  
644 J. and Miao, Y.: The Climatology of Low-Level Jet in Beijing and Guangzhou, China, *Journal of Geophysical*  
645 *Research: Atmosphere*, 123(5), 2816–2830, doi:10.1002/2017jd027321, 2018.

646 Mitchell, M. J., Arritt, R. W. and Labas, K.: A Climatology of the Warm Season Great Plains Low-Level Jet Using  
647 Wind Profiler Observations, *Weather and Forecasting*, 10(3), 576–591, doi:10.1175/1520-  
648 0434(1995)010<0576:acotws>2.0.co;2, 1995.

649 Montini, T. L., Jones, C. and Carvalho, L. M. V.: The South American Low-Level Jet: A New Climatology, Variability,  
650 and Changes, *Journal of Geophysical Research: Atmospheres*, 124(3), 1200–1218, doi:10.1029/2018jd029634, 2019.

651 Munday, C., Washington, R. and Hart, N.: African Low-Level Jets and Their Importance for Water Vapor Transport  
652 and Rainfall, *Geophysical Research Letters*, 48(1), doi:10.1029/2020gl090999, 2021.



---

653 Niu, G.-Y., Yang, Z.-L., Mitchell, K. E., Chen, F., Ek, M. B., Barlage, M., Kumar, A., Manning, K., Niyogi, D.,  
654 Rosero, E., Tewari, M. and Xia, Y.: The community Noah land surface model with multiparameterization options  
655 (Noah-MP): 1. Model description and evaluation with local-scale measurements, *Journal of Geophysical Research*,  
656 116(D12), doi:10.1029/2010jd015139, 2011.

657 Parish, T. R.: Forcing of the Summertime Low-Level Jet along the California Coast, *Journal of Applied Meteorology*,  
658 39(12), 2421–2433, doi:10.1175/1520-0450(2000)039<2421:fotsll>2.0.co;2, 2000.

659 Pu, B. and Cook, K. H.: Dynamics of the West African westerly jet, *Journal of Climate*, 23(23), 6263–6276,  
660 doi:10.1175/2010jcli3648.1, 2010.

661 Rahn, D. A. and Parish, T. R.: Diagnosis of the Forcing and Structure of the Coastal Jet near Cape Mendocino Using  
662 In Situ Observations and Numerical Simulations, *Journal of Applied Meteorology and Climatology*, 46(9), 1455–1468,  
663 doi:10.1175/jam2546.1, 2007.

664 Rife, D. L., Pinto, J. O., Monaghan, A. J., Davis, C. A. and Hannan, J. R.: Global Distribution and Characteristics of  
665 Diurnally Varying Low-Level Jets, *Journal of Climate*, 23(19), 5041–5064, doi:10.1175/2010jcli3514.1, 2010.

666 Saulo, C., Ruiz, J. and Skabar, Y. G.: Synergism between the Low-Level Jet and Organized Convection at Its Exit  
667 Region, *Monthly Weather Review*, 135(4), 1310–1326, doi:10.1175/mwr3317.1, 2007.

668 Shapiro, A., Fedorovich, E. and Rahimi, S.: A unified theory for the Great Plains Nocturnal low-level jet, *Journal of*  
669 *the Atmospheric Sciences*, 73(8), 3037–3057, doi:10.1175/jas-d-15-0307.1, 2016.

670 Smith, E. N., Gebauer, J. G., Klein, P. M., Fedorovich, E. and Gibbs, J. A.: The Great Plains Low-Level Jet during  
671 PECAN: Observed and Simulated Characteristics, *Monthly Weather Review*, 147(6), 1845–1869, doi:10.1175/mwr-  
672 d-18-0293.1, 2019.

673 Soares, P. M., Lima, D. C., Semedo, A., Cardoso, R. M., Cabos, W. and Sein, D. V.: Assessing the climate change  
674 impact on the North African offshore surface wind and coastal low-level jet using coupled and uncoupled regional  
675 climate simulations, *Climate Dynamics*, 52(11), 7111–7132, doi:10.1007/s00382-018-4565-9, 2018.

---

676 Stensrud, D. J.: Importance of Low-Level Jets to Climate: A Review, *Journal of Climate*, 9(8), 1698–1711,  
677 doi:10.1175/1520-0442(1996)009<1698:iolljt>2.0.co;2, 1996.

678 Sullivan, J. T., Rabenhorst, S. D., Dreessen, J., McGee, T. J., Delgado, R., Twigg, L. and Sumnicht, G.: Lidar  
679 observations revealing transport of O<sub>3</sub> in the presence of a nocturnal low-level jet: Regional implications for “next-  
680 day” pollution, *Atmospheric Environment*, 158, 160–171, doi:10.1016/j.atmosenv.2017.03.039, 2017.

681 Tang, Y., Winkler, J., Zhong, S., Bian, X., Doubler, D., Yu, L. and Walters, C.: Future changes in the climatology of  
682 the Great Plains low-level jet derived from fine resolution multi-model simulations, *Scientific Reports*, 7(1),  
683 doi:10.1038/s41598-017-05135-0, 2017.

684 Uccellini, L. W., Petersen, R. A., Kocin, P. J., Brill, K. F. and Tuccillo, J. J.: Synergistic Interactions between an  
685 Upper-Level Jet Streak and Diabatic Processes that Influence the Development of a Low-Level Jet and a Secondary  
686 Coastal Cyclone, *Monthly Weather Review*, 115(10), 2227–2261, doi:10.1175/1520-  
687 0493(1987)115<2227:sibaul>2.0.co;2, 1987.

688 Van de Wiel, B. J., Moene, A. F., Steeneveld, G. J., Baas, P., Bosveld, F. C. and Holtslag, A. A.: A conceptual view  
689 on inertial oscillations and nocturnal low-level jets, *Journal of the Atmospheric Sciences*, 67(8), 2679–2689,  
690 doi:10.1175/2010jas3289.1, 2010.

691 Walters, C. K. and Winkler, J. A.: Airflow Configurations of Warm Season Southerly Low-Level Wind Maxima in  
692 the Great Plains. Part I: Spatial and Temporal Characteristics and Relationship to Convection, *Weather and*  
693 *Forecasting*, 16(5), 513–530, doi:10.1175/1520-0434(2001)016<0513:acowss>2.0.co;2, 2001.

694 Walters, C. K., Winkler, J. A., Shadbolt, R. P., van Ravensway, J. and Bierly, G. D.: A Long-Term Climatology of  
695 Southerly and Northerly Low-Level Jets for the Central United States, *Annals of the Association of American*  
696 *Geographers*, 98(3), 521–552, doi:10.1080/00045600802046387, 2008.

697 Weide Luiz, E. and Fiedler, S.: Spatiotemporal observations of nocturnal low-level jets and impacts on wind  
698 power production, *Wind Energy Science*, 7(4), 1575–1591, doi:10.5194/wes-7-1575-2022, 2022.

---

699 Zhang, Y., Xue, M., Zhu, K. and Zhou, B.: What is the main cause of diurnal variation and nocturnal peak of summer  
700 precipitation in Sichuan Basin, China? the key role of boundary layer low-level jet inertial oscillations, *Journal of*  
701 *Geophysical Research: Atmospheres*, 124(5), 2643–2664, doi:10.1029/2018jd029834, 2019.

702 Zhong, S., Fast, J. D. and Bian, X.: A Case Study of the Great Plains Low-Level Jet Using Wind Profiler Network  
703 Data and a High-Resolution Mesoscale Model, *Monthly Weather Review*, 124(5), 785–806, doi:10.1175/1520-  
704 0493(1996)124<0785:acsotg>2.0.co;2, 1996.